8

Motion Control

Solution to Problem 8.1

The transfer function of the forward path of the scheme in Fig. 5.10 is

$$P(s) = C_P(s)M(s) = \frac{k_m K_P(1+sT_P)}{s^2(1+sT_m)},$$

being $C_P(s)$ the transfer function of he PI position controller and

$$M(s) = \frac{k_m}{s(1+sT_m)}.$$

The transfer function of the return path is

$$H(s) = k_{TP}.$$

It follows that the closed-loop input/output transfer function is

$$\frac{\Theta_m(s)}{\Theta_r(s)} = \frac{P(s)}{1+P(s)H(s)} = \frac{\dfrac{1}{k_{TP}}}{1+\dfrac{s^2(1+sT_m)}{k_m K_P k_{TP}(1+sT_P)}},$$

while the closed-loop disturbance/output transfer function is

$$\frac{\Theta_m(s)}{D(s)} = -\frac{M(s)}{1+P(s)H(s)} = -\frac{\dfrac{sR_a}{k_t K_P k_{TP}(1+sT_P)}}{1+\dfrac{s^2(1+sT_m)}{k_m K_P k_{TP}(1+sT_P)}}.$$

Solution to Problem 8.2

Operating by the rules for block reduction on the scheme in Fig. 5.11, it is worth moving the input to the block k_{TV} onto Θ_m and subtracting the

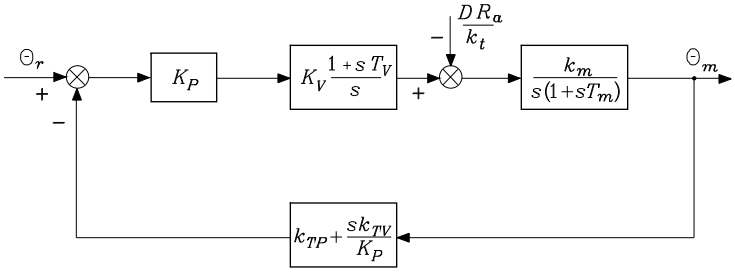

Fig. S8.1. Reduction on the block scheme of position and velocity feedback control

output to Θ_r. Then, the reduced block scheme of the system becomes that in Fig. S8.1.

The transfer function of the forward path is then

$$P(s) = K_P C_V(s) M(s) = \frac{k_m K_P K_V (1 + sT_V)}{s^2 (1 + sT_m)},$$

being $C_V(s)$ the transfer function of the PI velocity controller and $M(s)$ the transfer function of the actuator. The transfer function of the return path is

$$H(s) = k_{TP} \left(1 + s \frac{k_{TV}}{K_P k_{TP}} \right).$$

It follows that the closed-loop input/output transfer function with $T_V = T_m$ is

$$\frac{\Theta_m(s)}{\Theta_r(s)} = \frac{P(s)}{1 + P(s)H(s)} = \frac{\dfrac{1}{k_{TP}}}{1 + \dfrac{sk_{TV}}{K_P k_{TP}} + \dfrac{s^2}{k_m K_P k_{TP} K_V}}.$$

The closed-loop disturbance/output transfer function is

$$\frac{\Theta(s)}{D(s)} = -\frac{M(s)}{1 + P(s)H(s)} = -\frac{\dfrac{sR_a}{k_t K_P k_{TP} K_V (1 + sT_m)}}{1 + \dfrac{sk_{TV}}{K_P k_{TP}} + \dfrac{s^2}{k_m K_P k_{TP} K_V}}.$$

Solution to Problem 8.3

First, it is worth observing that the block scheme of Fig. 8.9 has been obtained from the scheme of Fig. 8.6 operating by the usual rules for block reduction. In particular, the input to the block k_{TA} has been moved onto $\dot{\Theta}_m$, while the output to the same block has been moved onto the output of $C_A(s)$. Likewise, the input to the block k_{TV} has been moved onto Θ_m, while the output to the

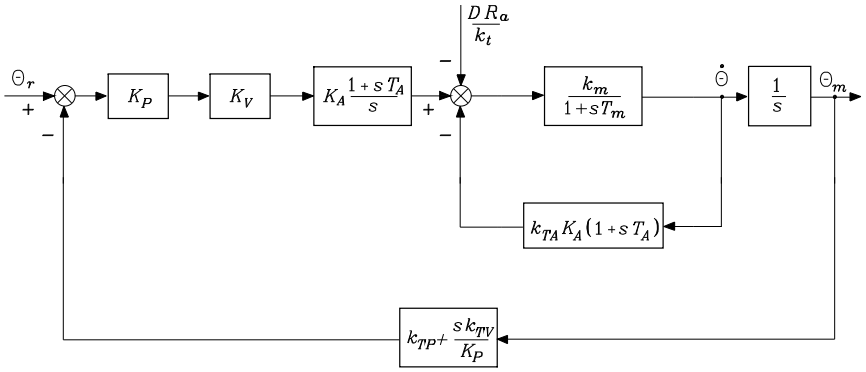

Fig. S8.2. Reduction on the block scheme of position, velocity and acceleration feedback control

same block has been moved onto the input to K_P; then, the resulting two blocks in parallel have been summed giving $(k_{TP} + sk_{TV}/K_P)$. Solving the inmost feedback loop gives the transfer function

$$sM(s) = \frac{\dfrac{k_t}{sR_aI}}{1 + \dfrac{k_t k_v}{sR_aI}} = \frac{\dfrac{1}{k_v}}{1 + \dfrac{sR_aI}{k_v k_t}} = \frac{k_m}{1 + sT_m},$$

and thus the block scheme of the system becomes that in Fig. S8.2.

Solving the inner feedback loop gives the transfer function

$$\begin{aligned} G'(s) &= \frac{\dfrac{k_m}{1+sT_m}}{1 + \dfrac{k_m k_{TA} K_A (1+sT_A)}{(1+sT_m)}} \\ &= \frac{k_m}{(1 + k_m K_A k_{TA}) \left(1 + \dfrac{sT_m \left(1 + k_m K_A k_{TA} \dfrac{T_A}{T_m} \right)}{(1 + k_m K_A k_{TA})} \right)}, \end{aligned}$$

and thus the block scheme of the system becomes that in Fig. S8.3.

The transfer function of the forward path is then

$$P(s) = \frac{K_P K_V C_A(s) G'(s)}{s} = \frac{K_P K_V K_A (1+sT_A)}{s^2} G'(s).$$

The transfer function of the return path is

$$H(s) = k_{TP} \left(1 + \frac{s k_{TV}}{K_P k_{TP}} \right).$$

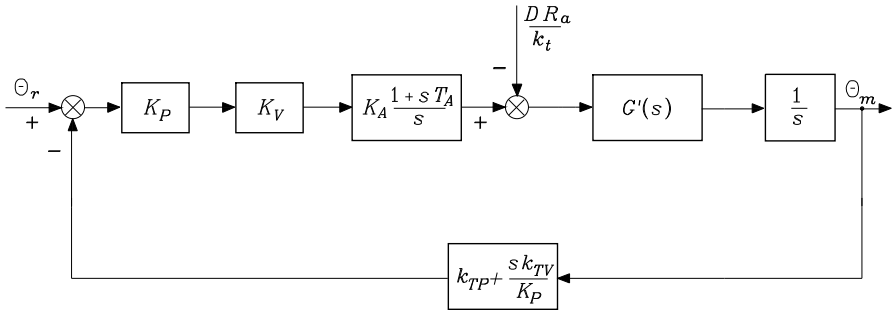

Fig. S8.3. Further reduction on the block scheme of position, velocity and acceleration feedback control

It follows that the closed-loop input/output transfer function with $T_A = T_m$ is

$$\frac{\Theta_m(s)}{\Theta_r(s)} = \frac{P(s)}{1+P(s)H(s)} = \frac{\dfrac{1}{k_{TP}}}{1+\dfrac{sk_{TV}}{K_P k_{TP}} + \dfrac{s^2(1+k_m K_A k_{TA})}{k_m K_P k_{TP} K_V K_A}},$$

while the closed-loop disturbance/output transfer function is

$$\frac{\Theta_m(s)}{D(s)} = -\frac{\dfrac{G'(s)}{s}}{1+P(s)H(s)} = -\frac{\dfrac{sR_a}{k_t K_P k_{TP} K_V K_A (1+sT_A)}}{1+\dfrac{sk_{TV}}{K_P k_{TP}} + \dfrac{s^2(1+k_m K_A k_{TA})}{k_m K_P k_{TP} K_V K_A}}.$$

Solution to Problem 8.4

With the given data, the condition $F_m \ll k_v k_t / R_a$ is verified and $k_m = 2\,\text{rad}/(\text{V}\cdot\text{s})$, $T_m = 7.2\,\text{s}$, $k_{TP} = 1$. The closed-loop input/output transfer function is

$$W(s) = \frac{(1+sT_P)}{1+sT_P + \dfrac{s^2(1+sT_m)}{k_m K_P k_{TP}}}.$$

Choosing $T_P = 10T_m = 72\,\text{s}$ leads to the root locus in Fig. S8.4 as a function of the gain $K' = 20K_P$.

If a damping ratio $\zeta = 0.4$ is desired, the resulting controller gain is $K_P = 0.0013$. For such value, two complex poles $(-0.062, \pm j0.142)$ and a real pole (-0.015) are obtained. Hence, the above transfer function can be written as

$$W(s) = \frac{(1+72s)}{(1+5.161s+41.62s^2)(1+66.66s)}.$$

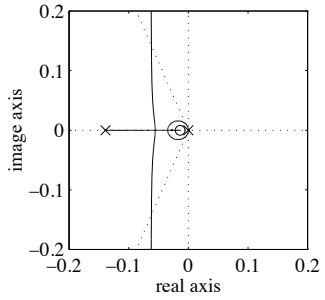

Fig. S8.4. Root locus for the position feedback control scheme

Correspondingly, the disturbance rejection factor is $X_R = 0.0013$, while an estimate of the output recovery time is $T_R = 72\,\mathrm{s}$. These values reveal the poor disturbance rejection performance of the closed-loop system under simple position feedback control.

Solution to Problem 8.5

With the given data, the condition $F_m \ll k_v k_t / R_a$ is verified and $k_m = 2\,\mathrm{rad/(V \cdot s)}$, $T_m = 7.2\,\mathrm{s}$, $k_{TP} = 1$, $k_{TV} = 1$. Choosing $T_V = T_m$ yields the closed-loop input/output transfer function

$$W(s) = \frac{1}{1 + \dfrac{s}{K_P} + \dfrac{s^2}{2K_P K_V}}.$$

With the given specifications for ζ and ω_n, the controller gains can be determined according to (8.30) and (8.31), giving $K_P = 25$ and $K_V = 8$, and thus the above transfer function becomes

$$W(s) = \frac{1}{1 + 0.04s + 0.0025s^2}$$

which has two complex poles $(-8, \pm j18.33)$. Correspondingly, the disturbance rejection factor is $X_R = 200$, while an estimate of the output recovery time is $T_R = 7.2\,\mathrm{s}$. These values reveal the good disturbance rejection performance of the closed-loop system under position and velocity feedback control; however, it is not possible to further decrease the output recovery time which is limited by the time constant T_m of the drive system.

Solution to Problem 8.6

With the given data, the condition $F_m \ll k_v k_t / R_a$ is verified and $k_m = 2\,\mathrm{rad/(V \cdot s)}$, $T_m = 7.2\,\mathrm{s}$, $k_{TP} = 1$, $k_{TV} = 1$, $k_{TA} = 1$. Choosing $T_A = T_m$ yields the closed-loop input/output transfer function

$$W(s) = \frac{1}{1 + \dfrac{s}{K_P} + \dfrac{s^2(1+2K_A)}{2K_P K_V K_A}}.$$

With the given specifications for ζ, ω_n and X_R, the controller gains can be determined according to (8.39), (8.40), (8.41) giving $K_P = 25$, $K_V = 32$, $K_A = 0.5$, and thus the above transfer function becomes

$$W(s) = \frac{1}{1 + 0.04s + 0.0025s^2}$$

which is the same transfer function of the previous problem. Remarkably, in the case of position, velocity and acceleration feedback control, the disturbance rejection performance is improved in terms of X_R, although the output recovery time T_R is still the same as in the previous case. Finally, in order to reconstruct acceleration from velocity measurement, a first-order filter as in Fig. 8.11 can be used. With the given ζ and ω_n, the closed-loop system bandwidth is $\omega_3 = 26.84\,\mathrm{rad/s}$, and then the filter bandwidth shall be chosen wide enough with respect to the drive system bandwidth, e.g., $\omega_{3f} = k_f = 400\,\mathrm{rad/s}$.

Solution to Problem 8.7

As for the block scheme in Fig. 8.12, where the saturation block can be neglected, it is worth moving both the output of the block T_m/k_m and the output of the block $1/k_m$ onto the input to the block $k_P(1 + sT_P)/s$; also the quantities $\dot{\Theta}_d$ and $\ddot{\Theta}_d$ can be generated from Θ_d as $s\Theta_d$ and $s^2\Theta_d$, respectively. Therefore, the reduced block scheme becomes that in Fig. S8.5.

The relationship between the desired input and the new reference input is then

$$\begin{aligned}\Theta'_r(s) &= \left(k_{TP} + \left(\frac{s^2 T_m}{k_m} + \frac{s}{k_m}\right)\frac{s}{K_P(1+sT_P)}\right)\Theta_d(s) \\ &= \left(k_{TP} + \frac{s^2(1+sT_m)}{k_m K_P(1+sT_P)}\right)\Theta_d(s).\end{aligned}$$

As for the block scheme in Fig. 8.13, where the saturation block can be neglected, it is worth moving both the output of the block $1/k_m K_V$ and the output of the block k_{TV} onto the input to the block K_P; as above, the quantities $\dot{\Theta}_d$ and $\ddot{\Theta}_d$ can be generated from Θ_d as $s\Theta_d$ and $s^2\Theta_d$, respectively. Therefore, the reduced block scheme becomes that in Fig. S8.6.

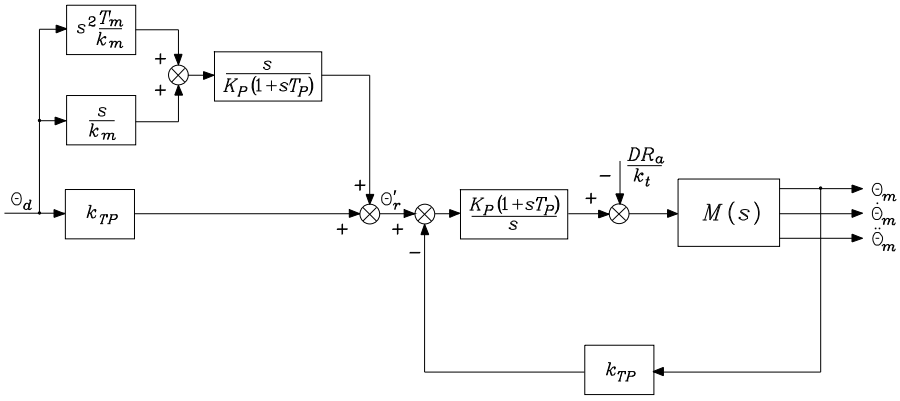

Fig. S8.5. Reduction on the block scheme of position feedback control with decentralized feedforward compensation

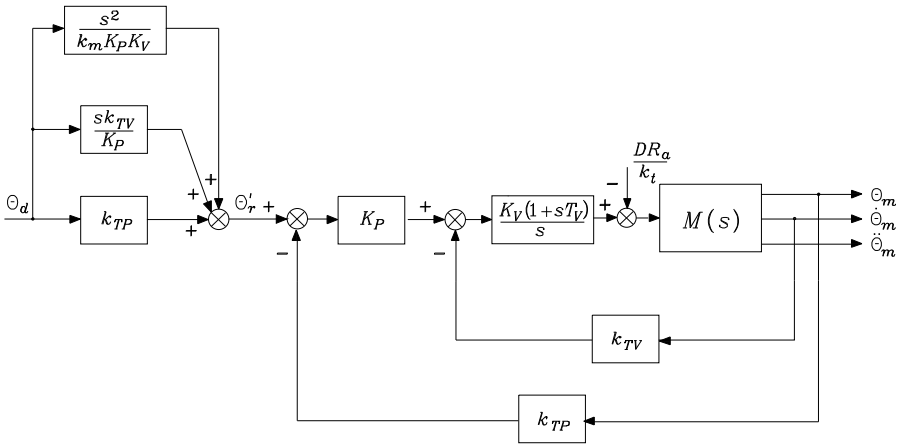

Fig. S8.6. Reduction on the block scheme of position and velocity feedback control with decentralized feedforward compensation

The relationship between the desired input and the new reference input is then

$$\Theta'_r(s) = \left(k_{TP} + \frac{sk_{TV}}{K_P} + \frac{s^2}{k_m K_P K_V}\right)\Theta_d(s).$$

As for the block scheme in Fig. 8.14, where the saturation block can be neglected, it is worth moving both the output of the block $(k_{TA} + 1/k_m K_A)$ and the output of the block k_{TV} onto the input to the block K_P; again, the quantities $\dot{\Theta}_d$ and $\ddot{\Theta}_d$ can be generated from Θ_d as $s\Theta_d$ and $s^2\Theta_d$, respectively. Therefore, the reduced block scheme becomes that in Fig. S8.7.

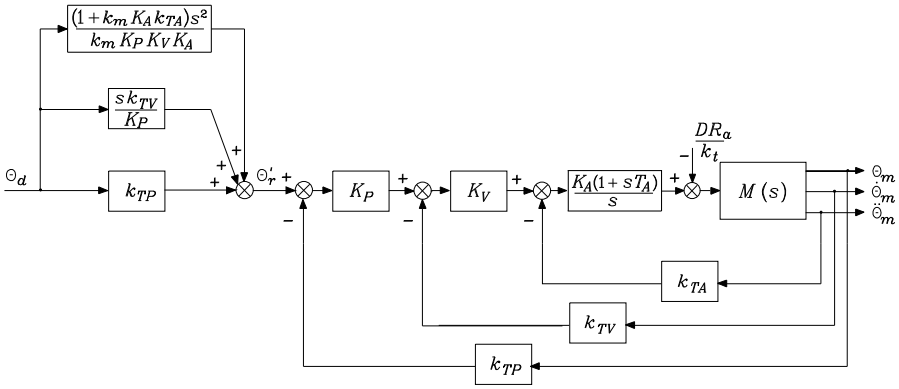

Fig. S8.7. Reduction on the block scheme of position, velocity and acceleration feedback control with decentralized feedforward compensation

The relationship between the desired input and the new reference input is then

$$\Theta'_r(s) = \left(k_{TP} + \frac{s k_{TV}}{K_P} + \frac{(1 + k_m K_A k_{TA}) s^2}{k_m K_P K_V K_A} \right) \Theta_d(s).$$

Solution to Problem 8.8

The block scheme in Fig. 8.15 is clearly equivalent to that in Fig. 8.12, since the block $K_P(1 + sT_P)/s$ can be split into two blocks in parallel, i.e., $K_P T_P$ and K_P/s.

Concerning the block scheme in Fig. 8.28, it is worth considering the input U and the output Y of the block $K_V(1 + sT_V)/s$. By neglecting the effect of the saturation block and setting $E = k_{TP}(\Theta_d - \Theta_m)$, the input U is given by

$$\begin{aligned} U &= K_P E + k_{TV}(\dot{\Theta}_d - \dot{\Theta}_m) + \frac{1}{k_m K_V} \ddot{\Theta}_d \\ &= K_P \left(1 + \frac{k_{TV}}{K_P k_{TP}} s \right) E + \frac{1}{k_m K_V} \ddot{\Theta}_d. \end{aligned}$$

Then the output can be expressed ($T_V = T_m$) as

$$\begin{aligned} Y &= \frac{K_V(1 + sT_V)}{s} \left(K_P \left(1 + \frac{k_{TV}}{K_P k_{TP}} s \right) E + \frac{1}{k_m K_V} \ddot{\Theta}_d \right) \\ &= K_P K_V \left(\frac{1}{s} + T_V \right) \left(1 + \frac{k_{TV}}{K_P k_{TP}} s \right) E + \frac{1}{k_m} \left(\frac{1}{s} + T_m \right) \ddot{\Theta}_d \\ &= \left(K_P K_V T_V + \frac{K_V k_{TV}}{k_{TP}} + \frac{K_P K_V}{s} + \frac{K_V T_V k_{TV}}{k_{TP}} s \right) E + \frac{1}{k_m} \dot{\Theta}_d + \frac{T_m}{k_m} \ddot{\Theta}_d \end{aligned}$$

corresponding to the block scheme in Fig. 8.16.

In a similar way, concerning the block scheme in Fig. 8.29, it is worth considering the input U and the output Y of the block $K_A(1 + sT_A)/s$. By neglecting the effect of the saturation blocks and setting $E = k_{TP}(\Theta_d - \Theta_m)$, the input U is given by

$$\begin{aligned} U &= K_V \left(K_P E + k_{TV}(\dot{\Theta}_d - \dot{\Theta}_m) \right) + \left(k_{TA} + \frac{1}{k_m K_A} \right) \ddot{\Theta}_d - k_{TA} \ddot{\Theta}_m \\ &= \left(K_P K_V + \frac{K_V k_{TV}}{k_{TP}} s + \frac{k_{TA}}{k_{TP}} s^2 \right) E + \frac{1}{k_m K_A} \ddot{\Theta}_d. \end{aligned}$$

Then the output can be expressed ($T_A = T_m$) as

$$\begin{aligned} Y &= K_A \left(\frac{1}{s} + T_A \right) \left(\left(K_P K_V + \frac{K_V k_{TV}}{k_{TP}} s + \frac{k_{TA}}{k_{TP}} s^2 \right) E + \frac{1}{k_m K_A} \ddot{\Theta}_d \right) \\ &= \left(K_P K_V K_A T_A + \frac{K_V k_{TV} K_A}{k_{TP}} + \frac{K_P K_V K_A}{s} \right. \\ &\quad \left. + \left(\frac{K_V k_{TV} K_A T_A + K_A k_{TA}}{k_{TP}} \right) s + \frac{K_A T_A k_{TA}}{k_{TP}} s^2 \right) E \\ &\quad + \frac{1}{k_m} \dot{\Theta}_d + \frac{T_m}{k_m} \ddot{\Theta}_d \end{aligned}$$

corresponding to the block scheme in Fig. 8.17.

Solution to Problem 8.9

From (8.75), the following matrix inequality can be written:

$$B_m \boldsymbol{I} \leq \boldsymbol{B}^{-1} \leq B_M \boldsymbol{I}$$

where all three matrices are positive definite. Setting

$$\widehat{\boldsymbol{B}} = \frac{2}{B_M + B_m} \boldsymbol{I},$$

which is positive definite, allows writing the matrix inequality

$$\frac{2B_m}{B_M + B_m} \boldsymbol{I} \leq \boldsymbol{B}^{-1} \widehat{\boldsymbol{B}} \leq \frac{2B_M}{B_M + B_m} \boldsymbol{I}.$$

Subtracting the identity matrix from each term gives

$$-\alpha \boldsymbol{I} \leq \boldsymbol{B}^{-1} \widehat{\boldsymbol{B}} - \boldsymbol{I} \leq \alpha \boldsymbol{I}$$

where

$$\alpha = \frac{B_M - B_m}{B_M + B_m}$$

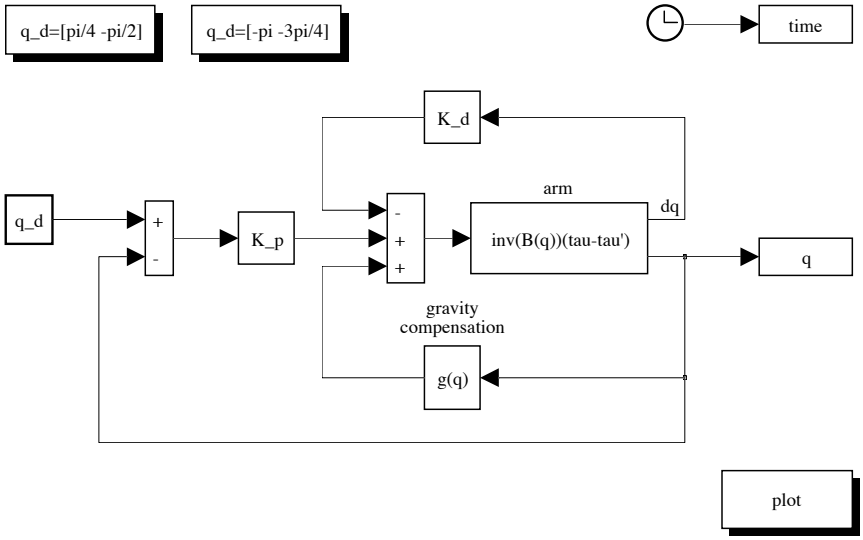

Fig. S8.8. SIMULINK block diagram of joint space PD control with gravity compensation

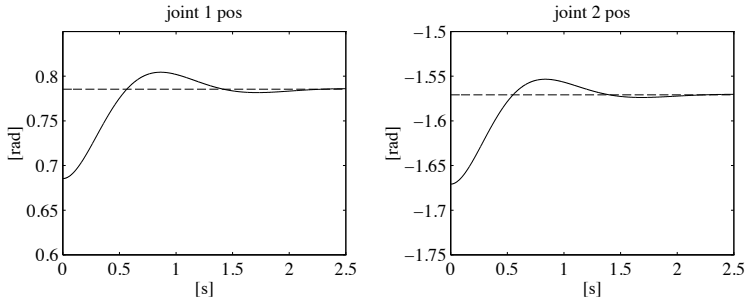

Fig. S8.9. Time history of the joint positions with joint space PD control with gravity compensation for the first posture

and $0 < \alpha < 1$. The matrix in the middle is lower bounded by a negative definite diagonal matrix and upper bounded by a positive definite diagonal matrix, where these two matrices have the same norm. Thus, it follows that

$$\|\boldsymbol{B}^{-1}\widehat{\boldsymbol{B}} - \boldsymbol{I}\| \leq \alpha.$$

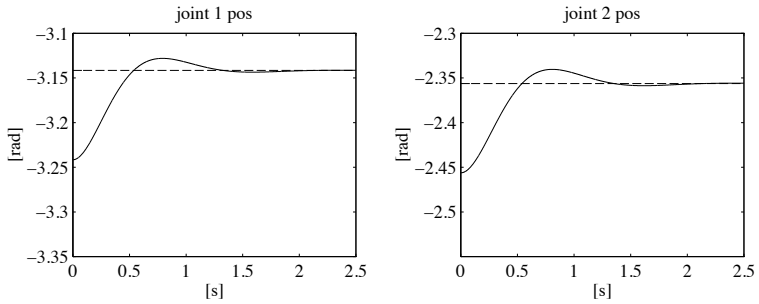

Fig. S8.10. Time history of the joint positions with joint space PD control with gravity compensation for the second posture

Solution to Problem 8.10

The control scheme in Fig. 8.20 is used with the same matrix gains as for case F in Sect. 8.7, i.e.,

$$\boldsymbol{K}_P = 3750\boldsymbol{I} \qquad \boldsymbol{K}_D = 750\boldsymbol{I}.$$

The initial arm postures for the two cases are chosen as $\boldsymbol{q} - [\,0.1 \quad 0.1\,]^T$. The various terms of the dynamic model are computed by using the minimum parameterization in the solution to Problem 7.4.

The resulting SIMULINK block diagram is shown in Fig. S8.8, where both desired postures can be assigned. The arm is simulated as a continuous-time system using a variable-step integration method with a maximum step size of 1 ms. All the blocks of the controller are simulated as discrete-time subsystems with the given sampling time of 1 ms.

The with the solution can be found in Folder `8_10`.

The resulting joint positions for the two postures are shown in Figs. S8.9 and S8.10, respectively. The dashed line indicates the desired joint position, while the solid line indicates the actual joint position. It can be seen that both postures are reached at steady state.

Solution to Problem 8.11

With reference to the dynamic model in the solution to Problem 7.4, the presence of a payload alters the dynamic parameters of augmented Link 2. Since the payload is a mass m_L concentrated at the tip, the only parameter that varies is the mass of the augmented link which becomes

$$m_2' = m_2 + m_L;$$

in fact, both the inertia first moment $m_2\ell_{C2}$ and inertia moment $\bar{I}_2$ remain the same because they are evaluated with respect to a frame located at the tip. Hence, only parameters π_1' and π_3' in (S7.2) have to be recomputed with the modified m_2'.

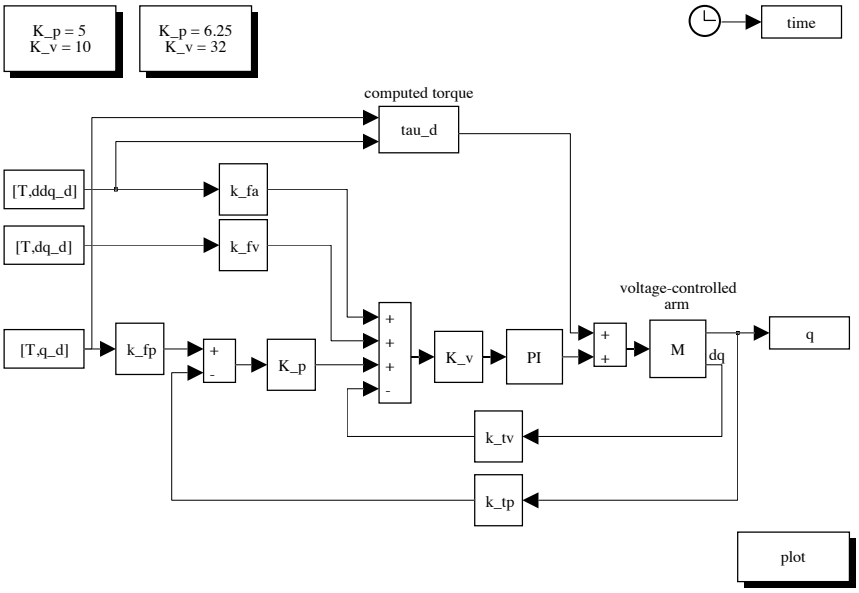

Fig. S8.11. SIMULINK block diagram of joint space computed torque control with feedforward compensation of the diagonal terms of the inertia matrix and of gravitational terms, and independent joint control with position and velocity feedback

The desired trajectories for the two joints are generated via trapezoidal velocity profiles with maximum velocities $\dot{q}_{c1} = 3\pi/4\,\text{rad/s}$ and $\dot{q}_{c2} = \pi/3\,\text{rad/s}$, respectively.

The control scheme in Fig. 8.19 is used with feedforward compensation of the diagonal terms of the inertia matrix and of gravitational terms. As for the decentralized controller, the independent joint control with position and velocity feedback in Fig. 5.11 is adopted.

Initially, the same gains for each joint servo are chosen as for case A in Sect. 8.7, i.e., ($k_{TP} = k_{TV} = 1$)

$$K_P = 5 \qquad K_V = 10,$$

corresponding to $\omega_n = 5\,\text{rad/s}$ and $\zeta = 0.5$, and thus to a closed-loop bandwidth $\omega_3 = 6.36\,\text{rad/s}$. This gives a disturbance rejection factor $X_R = 50$.

Then, by observing that the required trajectory is faster than the corresponding trajectory in Sect. 8.7, a larger bandwidth is imposed. Setting $\omega_n = 10\,\text{rad/s}$ and $\zeta = 0.8$ gives $\omega_3 = 10.78\,\text{rad/s}$. From (8.30) and (8.31), the gains become

$$K_P = 6.25 \qquad K_V = 32$$

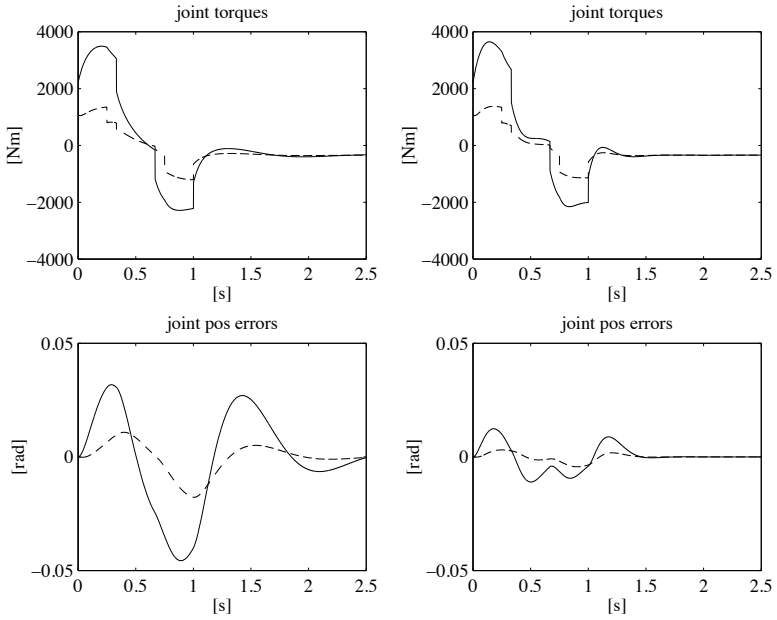

Fig. S8.12. Time history of the joint torques and position errors with joint space computed torque control with feedforward compensation of the diagonal terms of the inertia matrix and of gravitational terms, and independent joint control with position and velocity feedback; *left*—first choice of servo gains, *right*—second choice of servo gains

and, from (8.33), it is $X_R = 200$, i.e., a disturbance rejection factor which is four times as much as the previous one.

The resulting SIMULINK block diagram is shown in Fig. S8.11, where both choices of servo gains can be executed. The arm is voltage-controlled as in the scheme of Fig. 8.3 and is simulated as a continuous-time system using a variable-step integration method with a maximum step size of 1 ms. All the blocks of the controller are simulated as discrete-time subsystems with the given sampling time of 1 ms; in particular, the PI block is discretized assuming a zero-order hold on the inputs.

The files with the solution can be found in Folder `8_11`.

The resulting joint torques and position errors are shown in Fig. S8.12. The solid line refers to Joint 1, while the dashed line refers to Joint 2. It can be seen that the tracking performance with the second choice of the servo gains is considerably improved, at the expense of a sharper behaviour of joint torques, though.

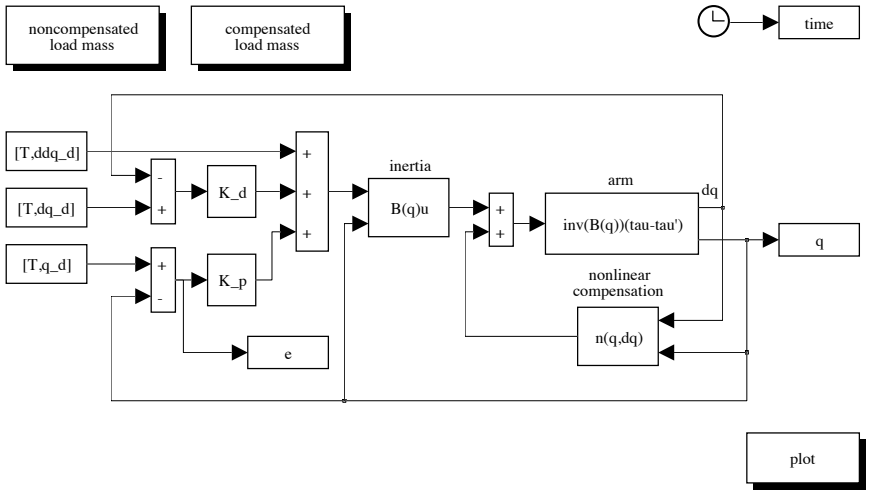

Fig. S8.13. SIMULINK block diagram of joint space inverse dynamics control

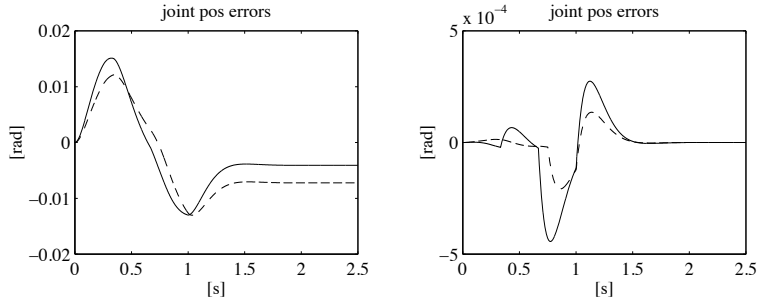

Fig. S8.14. Time history of the joint position errors with joint space inverse dynamics control; *left*—noncompensated load mass, *right*—compensated load mass

Solution to Problem 8.12

The modification of the dynamic model to account for the load mass and the generation of joint trajectories are accomplished as in the solution to Problem 8.11.

The control scheme in Fig. 8.22 is used where the matrix gains are chosen as

$$\boldsymbol{K}_P = 100\boldsymbol{I} \qquad \boldsymbol{K}_D = 16\boldsymbol{I}$$

corresponding to an error dynamics for both joints characterized by $\omega_{ni} = 10\,\mathrm{rad/s}$ and $\zeta_i = 0.8$ for $i = 1, 2$.

The resulting SIMULINK block diagram is shown in Fig. S8.13, where both the noncompensated load mass case and the compensated load mass case can

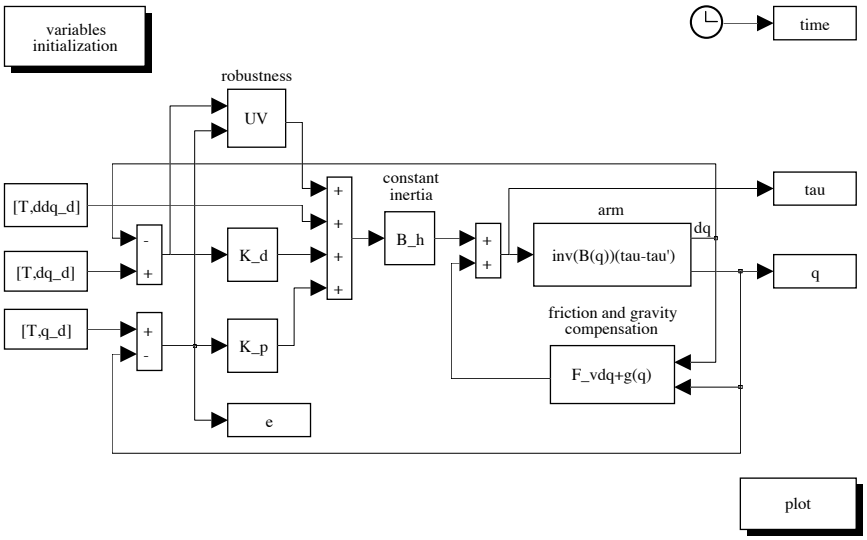

Fig. S8.15. SIMULINK block diagram of joint space robust control

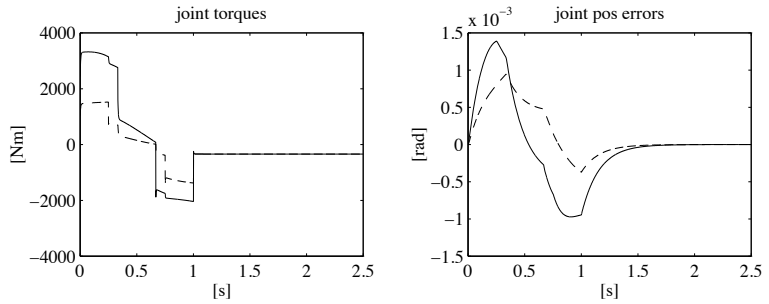

Fig. S8.16. Time history of the joint torques and position errors with joint space robust control

be executed. The arm is torque-controlled as in the scheme of Fig. 8.4 and is simulated as a continuous-time system using a variable-step integration method with a maximum step size of 0.1 ms. All the blocks of the controller are simulated as discrete-time subsystems with the given sampling time of 1 ms.

The files with the solution can be found in Folder `8_12`.

The resulting joint position errors in the two cases are shown in Fig. S8.14. The solid line refers to Joint 1, while the dashed line refers to Joint 2. It can be seen that the tracking performance is excellent when load mass is compensated, while it is degraded both during transient and at steady state

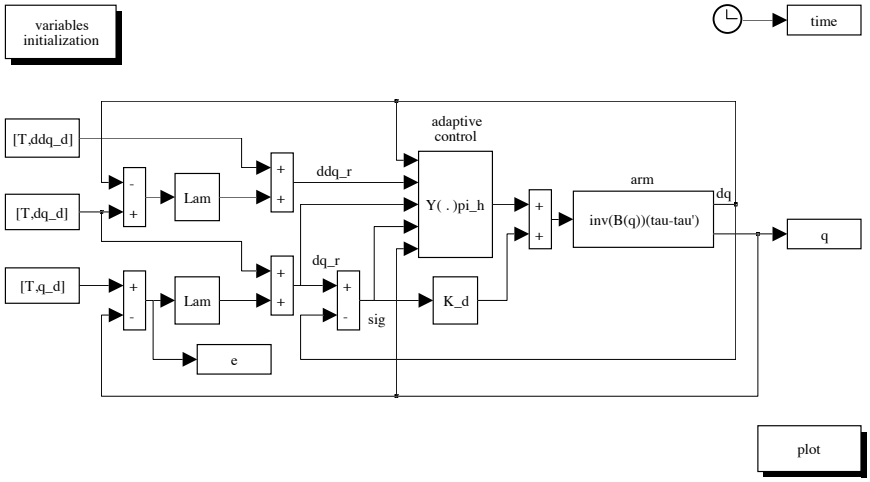

Fig. S8.17. SIMULINK block diagram of joint space adaptive control

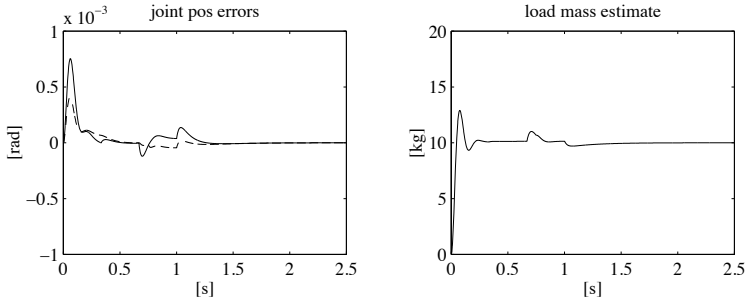

Fig. S8.18. Time history of the joint position errors and of the load mass estimate with joint space adaptive control

when the load mass is not compensated. Also, in the case of noncompensated load mass, steady-state errors occur.

Solution to Problem 8.13

The modification of the dynamic model to account for the load mass and the generation of joint trajectories are accomplished as in the solution to Problem 8.11.

The control scheme in Fig. 8.23 is used with constant inertia ($\widehat{\boldsymbol{B}} = \bar{\boldsymbol{B}}$) and compensation of friction and gravity ($\widehat{\boldsymbol{n}} = \boldsymbol{F}_v\dot{\boldsymbol{q}} + \boldsymbol{g}$). The gains defining the error dynamics are chosen as in the solution to Problem 8.12, i.e.,

$$\boldsymbol{K}_P = 100\boldsymbol{I} \qquad \boldsymbol{K}_D = 16\boldsymbol{I};$$

furthermore, the matrix $\boldsymbol{P}$ in (8.81) is chosen as

$$\boldsymbol{P} = \boldsymbol{I},$$

and the gain ρ and the thickness of the boundary layer in (8.89) are respectively chosen as

$$\rho = 70 \qquad \epsilon = 0.001.$$

The resulting SIMULINK block diagram is shown in Fig. S8.15. The arm is simulated as a continuous-time system using a variable step integration method with a maximum step size of 1 ms. All the blocks of the controller are simulated as discrete-time subsystems with the given sampling time of 1 ms.

The files with the solution can be found in Folder `8_13`.

The resulting joint torques and position errors are shown in Fig. S8.16. The solid line refers to Joint 1, while the dashed line refers to Joint 2. It can be seen that, in spite of the imperfect dynamic model compensation, the tracking performance is satisfactory, thanks to the use of the robustness action.

Solution to Problem 8.14

A minimum parameterization of the dynamic model is obtained as in the solution to Problem 7.4, with suitable modification of augmented Link 2 parameters as in the solution to Problem 8.11. The generation of joint trajectories is also accomplished as in the solution to Problem 8.11.

The control scheme in Fig. 8.26 is used. In terms of the new reference velocity and acceleration vectors in (8.92), the regressor in (S7.3) becomes

$$\begin{aligned}
y'_{11} &= a_1\ddot{\vartheta}_{r1} + gc_1 \\
y'_{12} &= \ddot{\vartheta}_{r1} \\
y'_{13} &= (2a_1c_2 + a_2)\ddot{\vartheta}_{r1} + (a_1c_2 + a_2)\ddot{\vartheta}_{r2} - a_1s_2\dot{\vartheta}_{r1}\dot{\vartheta}_2 - a_1s_2\dot{\vartheta}_1\dot{\vartheta}_{r2} - a_1s_2\dot{\vartheta}_2\dot{\vartheta}_{r2} \\
&\quad + gc_{12} \\
y'_{14} &= \ddot{\vartheta}_{r1} + \ddot{\vartheta}_{r2} \\
y'_{15} &= \ddot{\vartheta}_{r1} + k_{r2}\ddot{\vartheta}_{r2}
\end{aligned}$$

$$\begin{aligned}
y'_{21} &= 0 \\
y'_{22} &= 0 \\
y'_{23} &= (a_1c_2 + a_2)\ddot{\vartheta}_{r1} + a_2\ddot{\vartheta}_{r2} + a_1s_2\dot{\vartheta}_1\dot{\vartheta}_{r1} + gc_{12} \\
y'_{24} &= \ddot{\vartheta}_{r1} + \ddot{\vartheta}_{r2} \\
y'_{25} &= k_{r2}\ddot{\vartheta}_{r1} + k_{r2}^2\ddot{\vartheta}_{r2}.
\end{aligned}$$

In view of the presence of a concentrated tip load mass, the only variations occurring on the parameters in (S7.2) are:

$$\Delta\pi'_1 = a_1m_L \qquad \Delta\pi'_3 = a_2m_L.$$

Hence, the control law in (8.98) can be formally written as

$$\boldsymbol{u} = \boldsymbol{Y}'(\boldsymbol{q}, \dot{\boldsymbol{q}}, \dot{\boldsymbol{q}}_r, \ddot{\boldsymbol{q}}_r)\boldsymbol{\pi} + \boldsymbol{F}_v\dot{\boldsymbol{q}}_r + m_L\boldsymbol{y}_L + \boldsymbol{K}_D\boldsymbol{\sigma}$$

where $\boldsymbol{Y}'$ is computed as above and

$$\boldsymbol{y}_L = \begin{bmatrix} a_1 y'_{11} + a_2 y'_{13} \\ a_1 y'_{21} + a_2 y'_{23} \end{bmatrix},$$

being $\pi = m_L$ the only unknown parameter.

The gains are chosen as

$$\boldsymbol{\Lambda} = 10\boldsymbol{I} \qquad \boldsymbol{K}_D = 10000\boldsymbol{I} \qquad k_\pi = 0.005;$$

the initial estimate of π is set to 0, and the true value of m_L is utilized only to update the simulated arm model.

The resulting SIMULINK block diagram is shown in Fig. S8.17. The arm is simulated as a continuous-time system using a variable-step integration method with a maximum step size of 1 ms. All the blocks of the controller are simulated as discrete-time subsystems with the given sampling time of 1 ms.

The files with the solution can be found in Folder `8_14`.

The resulting joint position errors and load mass estimate are shown in Fig. S8.18. For the joint position errors, the solid line refers to Joint 1, while the dashed line refers to Joint 2. It can be seen that the tracking performance is satisfactory, thanks to the adaptive action on the load mass; in this case, the parameter estimate converges to the true value.

Solution to Problem 8.15

The modification of the dynamic model to account for the load mass is accomplished as in the solution to Problem 8.11.

The control scheme in Fig. 8.29 is used with the same matrix gains as for case K in Sect. 8.7, i.e.,

$$\boldsymbol{K}_P = 16250\boldsymbol{I} \qquad \boldsymbol{K}_D = 3250\boldsymbol{I}.$$

The initial tip positions for the two postures are chosen as $\boldsymbol{p} - [\,0.1 \quad 0.1\,]^T$.

The resulting SIMULINK block diagram is shown in Fig. S8.19, where both desired positions can be assigned. The arm is simulated as a continuous-time system using a vaiable-step integration method with a maximum step size of 1 ms. All the blocks of the controller are simulated as discrete-time subsystems with the given sampling time of 1 ms.

The files with the solution can be found in Folder `8_15`.

The resulting components of tip position for the two postures are shown in Figs. S8.20 and S8.21, respectively. The dashed line indicates the desired tip coordinate, while the solid line indicates the actual tip coordinate. It can be seen that both postures are reached at steady state.

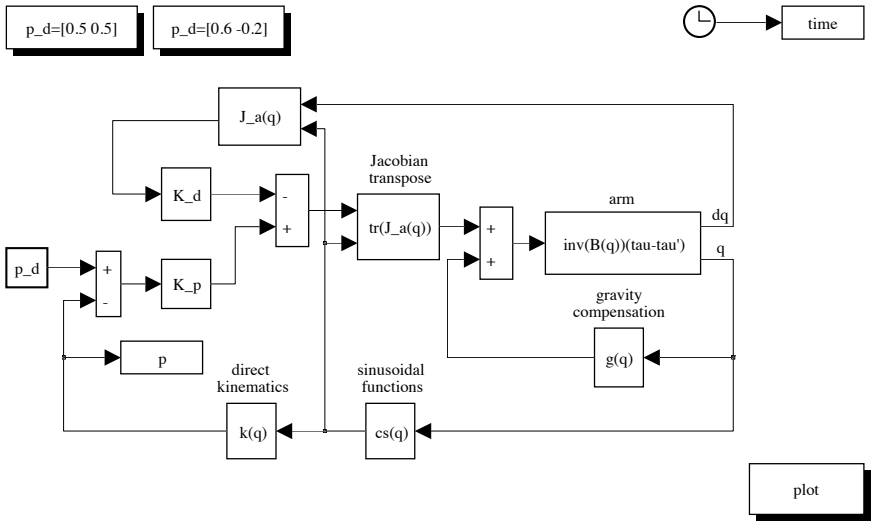

Fig. S8.19. SIMULINK block diagram of operational space PD control with gravity compensation

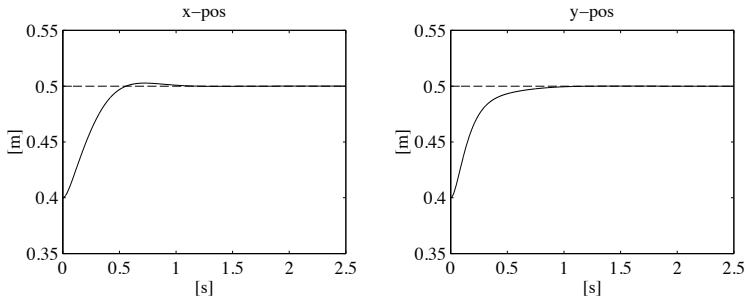

Fig. S8.20. Time history of the tip position components with operational space PD control with gravity compensation for the first posture

Solution to Problem 8.16

The modification of the dynamic model to account for the load mass is accomplished as in the solution to Problem 8.11. The desired tip trajectory is generated in terms of the path coordinate s via a trapezoidal velocity profile with maximum velocity $\dot{s}_c = 1.5$.

The control scheme in Fig. 8.30 is used with the matrix gains:

$$\boldsymbol{K}_P = 100\boldsymbol{I} \qquad \boldsymbol{K}_D = 16\boldsymbol{I}.$$

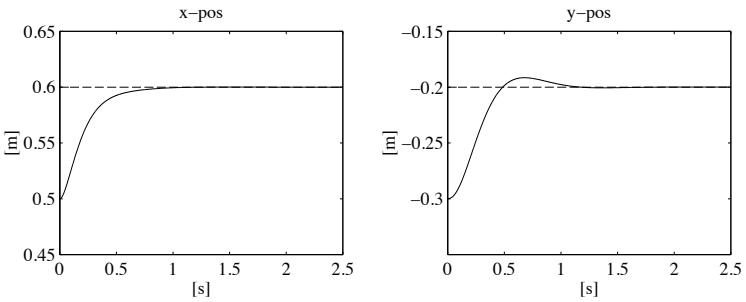

Fig. S8.21. Time history of the tip position components with operational space PD control with gravity compensation for the second posture

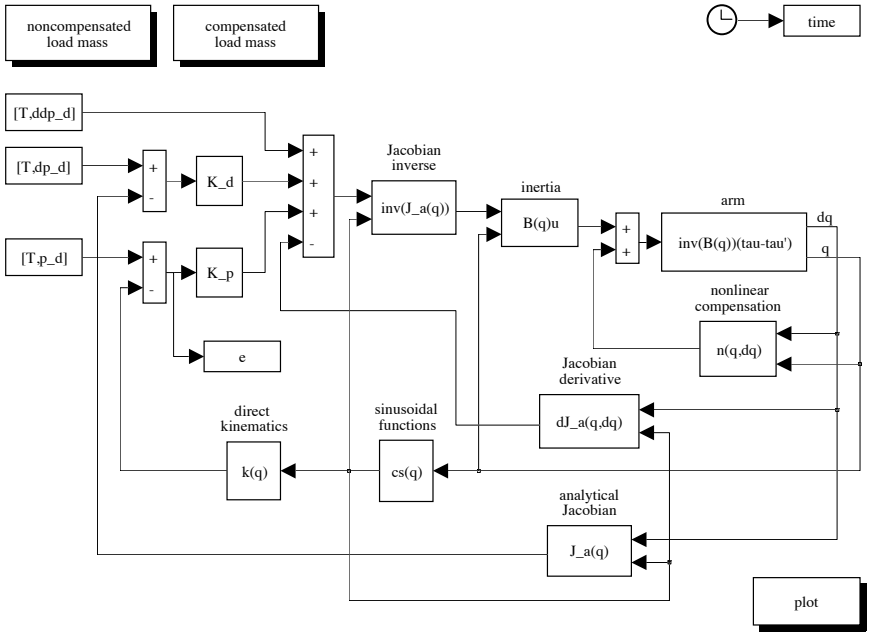

Fig. S8.22. SIMULINK block diagram of operational space inverse dynamics control

The resulting SIMULINK block diagram is shown in Fig. S8.22, where both the noncompensated load mass case and the compensated load mass case can be executed. The arm is simulated as a continuous-time system using a variable-step integration method with a maximum step size of 1 ms. All the blocks of the controller are simulated as discrete-time subsystems with the given sampling time of 1 ms.

The files with the solution can be found in Folder `8_16`.

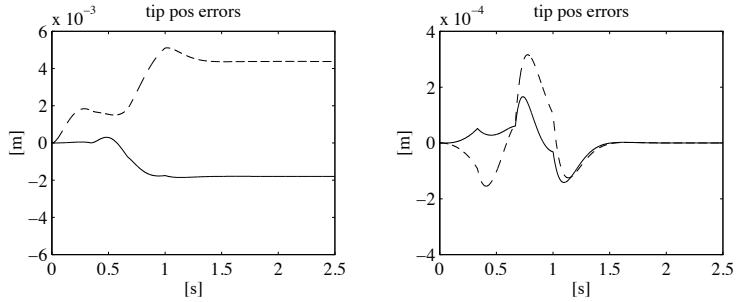

Fig. S8.23. Time history of the components of tip position error with operational space inverse dynamics control; *left*—noncompensated load mass, *right*—compensated load mass

The resulting components of tip position error in the two cases are shown in Fig. S8.23. The solid line refers to x component, while the dashed line refers to y component. It can be seen that the performance is excellent when the load mass is compensated, while it is degraded both during transient and at steady state when the load mass is not compensated.